

Diffusion-facilitated transport of self-driven particles in polycrystalline structures

Takahiro Ezaki^{1,*}, Katsuhiro Nishinari^{1,2}, and Yasunobu Ando³

¹Research Center for Advanced Science and Technology, The University of Tokyo, 4-6-1 Komaba, Meguro-ku, Tokyo 153-8904, Japan

²Department of Aeronautics and Astronautics, School of Engineering, The University of Tokyo, 7-3-1 Hongo, Bunkyo-ku, Tokyo 113-8656, Japan

³Laboratory for Chemistry and Life Science, Tokyo Institute of Technology, 4259 Nagatsuta-cho, Midori-ku, Yokohama 226-8503, Japan



(Received 28 May 2024; accepted 17 July 2024; published 8 August 2024)

We study particle transport in a polycrystalline system with mesoscale regular structures, which was inspired by ionic transport in solids. We found a novel type of congestion dynamics in which the density of particles spontaneously became strongly inhomogeneous with increasing driving force field and inverse temperature, leaving strongly localized pathways that allowed for substantial particle current. Consequently, particle current was maximized at a certain driving force strength and inverse temperature, which effectively avoided overcrowding of particles via a moderate level of diffusion. Our findings not only extend the theory of collective transport of self-propelled particles but also provide a baseline for understanding the transport properties of real polycrystalline systems, including superionic materials.

DOI: [10.1103/PhysRevResearch.6.L032032](https://doi.org/10.1103/PhysRevResearch.6.L032032)

Introduction. A wide range of problems, spanning biological transport processes, vehicular traffic, and enzymatic chemical reactions, among others, can be understood via transport phenomena involving interacting particles [1–3]. They are often modeled by self-propelled particles stochastically moving in a channel represented by a one-dimensional (1D) lattice, which is referred to as the asymmetric simple exclusion process (ASEP) [4,5]. Interparticle interactions and boundary conditions have been shown to considerably affect particle currents and density distributions, which are quantities of primary interest in such systems, often accompanied by phase transitions. Theoretical studies have also revealed the effects of particle adsorption and desorption [6–9], local defects [10–12], multiple channels [13,14], and network structures [9,15,16], among others, on particle currents and density distributions. While these studies have established the fundamentals of the physics of complex transports, the interplay between the structural complexity of channels and interparticle interactions has remained largely unexplored. For example, studies have been conducted on the junctions of multiple channels [17–19] and random network structures [15,20], but only few studies have investigated the effects of channels with specific mesoscopic or macroscopic structures.

Such a factor often plays a crucial role in various systems, involving materials with macroscopic molecular structure. For example, the slowdown of enzymatic reactions in degradation of crystalline cellulose was explained by the spatial structure

of channels [3]. Ionic transport in solids is another potentially relevant problem. Superionic conductors are a class of materials that exhibit high ionic conductivity, even comparable to that of liquid electrolytes [21–23]. In particular, stable ones are used in solid-state batteries, fuel cells, and sensors because of their remarkable ionic conductivity, which are referred to as solid electrolytes [24]. The crystalline structure of a superionic conductor features a rigid lattice of immobile metal cations and anions (i.e., framework). This lattice includes interstitial sites or vacancies that form pathways and channels for mobile ions, hence enabling high ionic conductivity. The arrangement and connectivity of these pathways are considered essential for the material's conductivity properties. While progress has been made vis-à-vis the design principle of materials with high ionic conductivity [25,26], a unified understanding of the ideal material structure has remained elusive. One of the obstacles is the complex many-body interactions that involve both mobile particles and structured frameworks. Common numerical methods that incorporate the dynamics of multiple ions, including molecular dynamics [27,28], are generally limited in terms of the number of ions and time scales by their computational costs, preventing the analysis of such collective motions. In other words, we currently lack a theoretical framework for describing this mesoscale physics.

Herein, we studied transport dynamics of self-propelled particles in channels locally structured within polycrystals. A 2D region was divided into randomly generated grains with random orientation, in which parallel channels were regularly arranged. Such a polycrystalline structure is common among a class of superionic conductors [29–31], including silver iodide (AgI), which is one of the classical examples. In such systems, the pathways for particle flow are complex, making it difficult to predict and understand the system behavior using, for example, a simple mean-field description. In this study, we

*Contact author: tkezaki@ecc.g.u-tokyo.ac.jp

Published by the American Physical Society under the terms of the [Creative Commons Attribution 4.0 International license](https://creativecommons.org/licenses/by/4.0/). Further distribution of this work must maintain attribution to the author(s) and the published article's title, journal citation, and DOI.

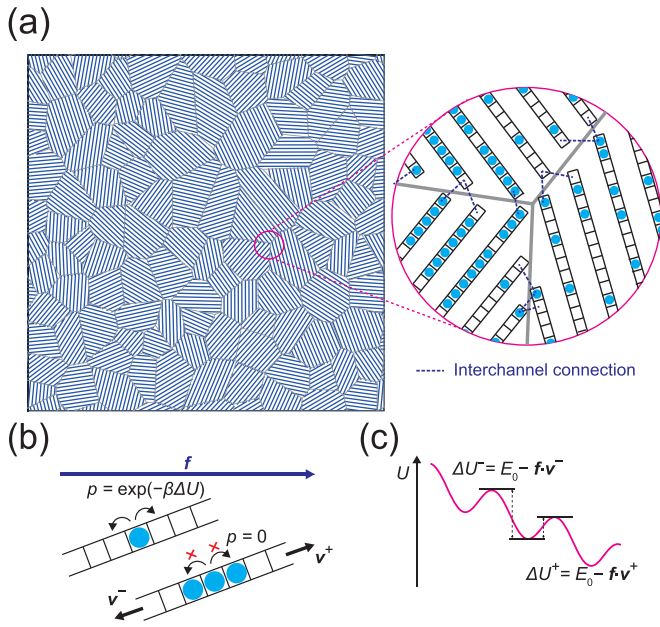


FIG. 1. (a) The polycrystalline structure model. (b) Definition of particle motion within channels. (c) Energy barrier and driving field vector f projected onto channel orientation.

have not pursued detailed modeling of any specific material or system. Instead, we have focused on the fundamental physics emerging from the interplay between assumed lattice structure and interparticle interactions in a bid to facilitate a general understanding of such systems.

Model. We first generated the polycrystalline structure as follows [Fig. 1(a)]. We randomly placed n points (x_i, y_i) ($i = 1, \dots, n$) in an $L \times L$ region, where n and L represents grain number and system length, respectively. Voronoi tessellation was employed to define the grains while assuming periodic boundary conditions. Controlling the minimum distance between the points to be αd , where $d = \sqrt{2L^2/\sqrt{3n}}$ represents the distance between adjacent points in the most dispersed n -point configuration, allowed us to tune the grain regularity via the parameter α [32]. Each grain i was assigned a random orientation angle θ_i . Channels were then generated for each grain as follows. First, we drew the line through (x_i, y_i) at angle θ_i that intersected the grain's Voronoi boundary. Sites of unit length were consecutively placed along a segment of this line, centered such that their centroid coincided with the segment's midpoint. Parallel channels were created by translating this line segment by distance λ . If the number of sites that can be accommodated along the line segment was less than l_{\min} , no channel was generated there. We fixed $L = 1000$ and $\lambda = l_{\min} = 10$ in this study. The distributions of the grain area, the number of edges in each grain boundary, and the channel length for various values of the parameters n and α are shown in Fig. S1 in the Supplemental Material [33]. In each channel, we defined the rightmost site in the x-axis direction as the *plus end* and the leftmost site as the *minus end*. Accordingly, we also defined the *plus direction* (characterized by the unit vector v^+) and the *minus direction* ($v^- (= -v^+)$).

The particle motion within the channels was defined as follows [Fig. 1(b)]. A particle hopped to a neighboring site

at rate $p = \exp(-\beta\Delta U)$ if that neighboring site was unoccupied, where β represents the inverse temperature and ΔU activation potential for a transition between the final and initial sites [23,34]. ΔU was given by the sum of base activation potential (E_0) and potential difference generated by a uniform driving field (f). We fixed $E_0 = 1$. The effect of the driving field depended on channel orientation angle θ_i , which was quantified by projection of the driving field vector on the unit direction vector, $f \cdot v^+$ (for the plus direction) or $f \cdot v^-$ (the minus direction) [Fig. 1(c)]. Without loss of generality, we set $f = f n_x$, where $f \in [0, \infty)$ and n_x represent the strength of driving field and a unit vector in the x-axis direction, respectively. At the sites at both ends of the channel, we identified the nearest site within other grains (not limited to boundary sites) and enabled a particle to move back and forth to the site as an adjacent site. The unit direction vector of the movement was defined as the difference in coordinates between the two sites (denoted by Δr) as $v = \Delta r / \|\Delta r\|$. For this transition, we defined the activation potential as $\Delta U = E_0 - f \cdot v$. In this manner, possible particle transitions in the system were defined. We labeled each transition by $k = 1, \dots, N_{\text{transition}}$. Noteworthy, the dynamics within each channel can be perceived as a specific case of the ASEP, except that particle hopping between channels was allowed at the sites in the bulk connected to a boundary site of another channel.

As the initial conditions, we generated $\bar{\rho} N_{\text{sites}}$ particles at random locations, where N_{sites} represents the number of sites in the system. At each time step to update time from t to $t + dt$, we randomly selected $N_{\text{transition}}$ transitions allowing for duplications from all the possible transitions and sequentially moved each particle in the specified site, if any, with probability $p_k dt$, provided the conditions for movement were satisfied. Herein, p_k represents the transition rate for transition k . dt was set to be the inverse of the maximum value of the transition rate in the system (i.e., $dt = 1/\max_k p_k$). Each experiment was run for 10 000 steps, and the current and density of particles were calculated as the average of the remaining 9 000 steps after excluding the initial 1 000 steps in which transient dynamics were observed.

Results. First, we focus on the density (denoted by ρ), current in the x-axis direction (J_x), and nondirected motion (D) of particles. The density of particles was computed for each channel by averaging the number of particles it contained over simulation time steps and dividing it by the number of sites in the channel. The motion of particles was separated into directed and nondirected components. The directed component was computed by counting the number of times particles moved in the plus and minus directions (denoted by c^+ and c^- , respectively) and calculating the net particle movement ($(c^+ - c^-) v^+$) per site per unit time. Its x-axis component was used as an indicator of the particle current induced by the potential field f . The undirected component was computed as the number of particle motions subtracted by that accounting for the directed motion (i.e., $c^+ + c^- - |c^+ - c^-|$) per site per unit time.

Figure 2(a) shows the spatial distribution of particle density for a single sample with an average particle density of $\bar{\rho} = 0.5$. Remarkably, the particles segregated into high-density (HD) channels and low-density (LD) channels, with a small number of channels exhibiting medium density (MD).

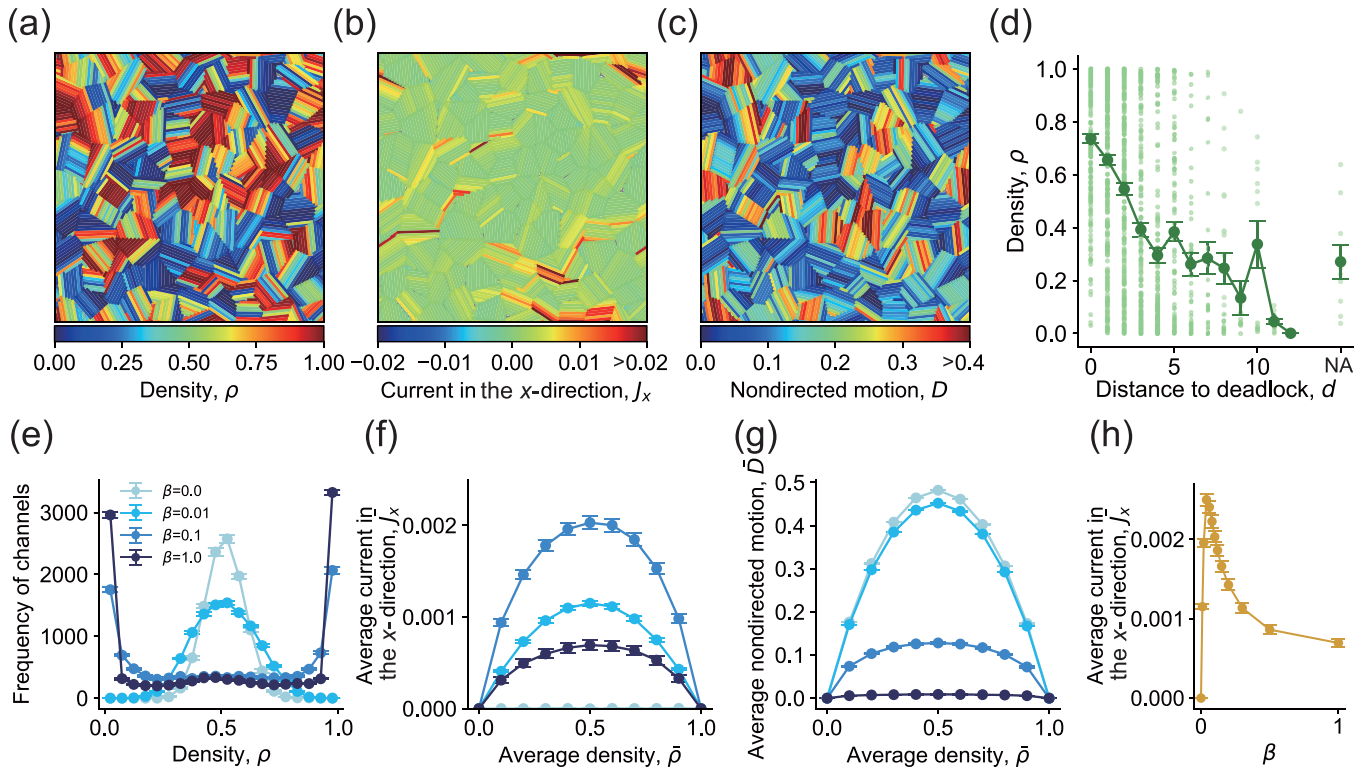


FIG. 2. (a)–(c) Spatial results for a single sample, where we set $f = 1$, $n = 100$, $\alpha = 0.5$, $\beta = 0.1$, and $\bar{\rho} = 0.5$. (a) Spatial distribution of particle density. (b) Current in the x-axis direction. (c) Nondirected motion. (d) Correlation between the density in the channel and the distance to a deadlock, d , for a single sample corresponding to (a)–(c). The channels that were not connected to any deadlocks are shown by NA. The small markers represent each channel, and the large markers and error bars represent the mean and standard error calculated over channels with the same d . (e) Density distributions at various inverse temperatures β at $\bar{\rho} = 0.5$. (f) Current in the x-axis direction versus average density for various β values. (g) Nondirected motion versus average density for various β values. (h) Current in the x-axis direction versus β for various average densities. The markers and error bars in (e)–(h) represent the mean and standard error calculated over 20 samples, respectively.

Figure 2(b) shows the current along the x-axis direction. While a positive current arises along a few channel paths, the overall current is considerably suppressed. The channels with substantial particle current consisted of strongly localized pathways. In contrast, channels oriented along the y axis, which contributed minimally to the x-axis current, exhibited pronounced nondirected motion [Fig. 2(c)].

The density segregation was attributed to pairs of channels connected with each other at their plus ends, which we referred to as the deadlock. In such channels, particles driven to the plus end become trapped, resulting in increased density [see also Fig. 1(a)]. Moreover, other channels connected to these HD channels by the plus end successively become congested via a cascading process, ultimately confining of the majority of the particles. To analyze this effect, we quantified the number of steps required to reach a deadlock via tracing from each channel’s plus end. This metric roughly accounted for the observed density profiles [Fig. 2(d)]. We also performed simulations under a control condition with all channels oriented along the x axis, where deadlocks were absent, and confirmed that strong density separation was not observed although local density inhomogeneities occurred due to variations in channel connectivity [Figs. S2(a)–S2(d) in the Supplemental Material [33]]. The angle of each channel alone could not explain the variations in the density distributions or the x-axis currents [Figs. S3(a) and S3(b) in

the Supplemental Material [33]]. However, channels forming deadlocks with a smaller angle difference tended to have higher particle densities [Fig. S3(d) in the Supplemental Material [33]].

Next, we investigated the temperature dependence of the system. We fixed $f = 1$, $n = 100$, and $\alpha = 0.5$ and varied β . Microscopically, $\beta = 0$ corresponds to $T = +\infty$, at which thermal fluctuations dominate and nondirected motion overwhelms the current, while for large β , the particle motion is strongly biased along the direction of the external field, suppressing nondirected motion. Figure 2(e) shows the density distribution across channels for an average density of $\bar{\rho} = 0.5$. Interestingly, for small β , a single-peaked distribution centered at approximately 0.5 was observed, whereas a clear segregation into low and high densities emerged with increasing β (see also Fig. S4 in Supplemental Materials [33]). Figures 2(f) and 2(g) show the current in the x-axis direction and nondirected motion, respectively, averaged over all channels, as a function of the average density. While the nondirected motion monotonically decreased with increasing β [Fig. 2(g)], the current in the x-axis direction first increased but then decreased at beyond a certain point of β [Figs. 2(f) and 2(h)]. For small β , randomness mitigated deadlocks but eliminated the driving force along the field direction. The effect of driving field became stronger and enhanced the current as β increased, but the negative impact of deadlocks

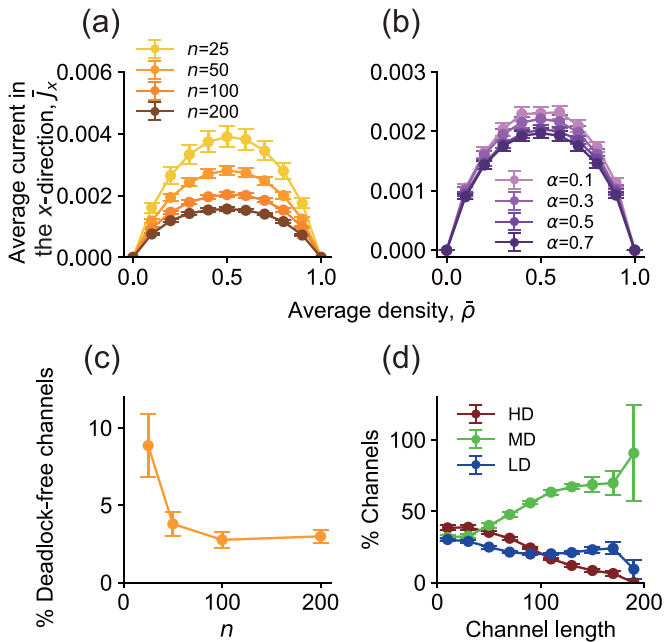


FIG. 3. Current in the x-axis direction for various values of (a) n and (b) α . (c) Percentage of deadlock-free channels for various n values. (d) Percentage of high-density (HD), medium-density (MD), and low-density (LD) channels conditioned by the channel length. The markers and error bars represent the mean and standard error, respectively. The parameter values were set to be $f = 1$, $n = 100$, $\alpha = 0.5$, and $\bar{\rho} = 0.5$ unless otherwise specified in each panel.

dominated beyond a certain value of β , resulting in a peak. Thus, an optimal inverse temperature existed that maximized the current in this systems. This result was preserved for various values of f [Fig. S5(a) in the Supplemental Material [33]]. Note that in the absence of deadlocks, we observed a monotonic increase in current as β increased [Fig. S2(e) in the Supplemental Material [33]]. For a fixed β , there existed an f value that maximized the current by yielding a moderate level of diffusion relative to driving force [Fig. S5(b) in the Supplemental Material [33]].

We also varied n and α to investigate the effects of grain size and variability thereof on the current of particles (Fig. 3; Figs. S6 and S7 in the Supplemental Material [33]). Decreasing n substantially increased the current [Fig. 3(a)], whereas decreasing α slightly increased the current [Fig. 3(b)]. We explain this behavior on the basis of two factors. The first and the more dominant factor is the number of deadlocks. The number

of boundaries decreased as n decreased, resulting in fewer deadlocks per unit area. The proportion of channels that did not reach a deadlock when tracing the plus ends became considerably larger when n was small [Fig. 3(c)]. Noteworthy, this metric did not considerably change with variations in α [Fig. S8(a) in the Supplemental Material]. The second factor is the average length of the channels. Longer channels were less likely to become HD or LD, leaving MD channels that contribute to the current [Fig. 3(d); see Figs. S8(b) and S8(c) in the Supplemental Material for the results classified by the orientation of channels [33]]. This is because longer channels are more likely to connect with other channels, allowing for particles to average out across multiple adjacent channels. Decreasing n and α both increased the proportion of such long channels [Figs. S1(c) and S1(f) in the Supplemental Material [33]]. Note that the number of short channels increased as α decreased as well, but its negative impacts were offset by the positive impacts of an increasing longer channels.

Discussions. We revealed a distinctive congestion pattern observed within channels embedded in polycrystalline structures. Substantial current was strongly localized along specific pathways, while numerous channels exhibited deadlocks and vacancies due to spontaneous density separation, or diffusion processes that did not contribute to the overall current. In addition, we observed an appropriate noise strength or force field strength that maximized the current by mitigating the density separation. While this study focused on a 2D system, we consider that the results, explained by the deadlock formation simply due to the angular relationship between connected channels, would persist in 3D systems as well.

We believe that our findings are not only theoretically intriguing but also useful as a baseline for understanding real systems. For example, in this study, the current increased as the grain number decreased because the negative effect of grain boundaries on particle current was reduced. However, the opposite pattern has been observed in several superionic conductors [30]. This suggests that there may be mechanisms to avoid deadlocks in such materials. For example, the grain boundaries, which have their own size, may act as channels of high conductivity. Combining mesoscale material simulations, such as the kinetic Monte Carlo (i.e., kMC) method [35–38], with our approach would be promising for quantitative analysis of real systems.

Acknowledgments. The authors thank Prof. Y. Tateyama for giving a general discussion on the field of solid-state ionics. This work was supported by Japan Society for the Promotion of Science (JSPS), Grants-in-Aid for Scientific Research (KAKENHI) Grant No. 24H02203.

- [1] D. Helbing, Traffic and related self-driven many-particle systems, *Rev. Mod. Phys.* **73**, 1067 (2001).
- [2] A. Schadschneider, D. Chowdhury, and K. Nishinari, *Stochastic Transport in Complex Systems: From Molecules to Vehicles* (Elsevier, Amsterdam, 2010).
- [3] T. Ezaki, K. Nishinari, M. Samejima, and K. Igarashi, Bridging the micro-macro gap between single-molecular behavior and bulk hydrolysis properties of cellulose, *Phys. Rev. Lett.* **122**, 098102 (2019).
- [4] G. Schütz and E. Domany, Phase transitions in an exactly soluble one-dimensional exclusion process, *J. Stat. Phys.* **72**, 277 (1993).
- [5] B. Derrida, An exactly soluble non-equilibrium system: The asymmetric simple exclusion process, *Phys. Rep.* **301**, 65 (1998).
- [6] A. Parmeggiani, T. Franosch, and E. Frey, Phase coexistence in driven one-dimensional transport, *Phys. Rev. Lett.* **90**, 086601 (2003).

- [7] A. Parmeggiani, T. Franosch, and E. Frey, Totally asymmetric simple exclusion process with Langmuir kinetics, *Phys. Rev. E* **70**, 046101 (2004).
- [8] T. Ezaki and K. Nishinari, Exact stationary distribution of an asymmetric simple exclusion process with langmuir kinetics and memory reservoirs, *J. Phys. A* **45**, 185002 (2012).
- [9] I. Neri, N. Kern, and A. Parmeggiani, Modeling cytoskeletal traffic: An interplay between passive diffusion and active transport, *Phys. Rev. Lett.* **110**, 098102 (2013).
- [10] S. A. Janowsky and J. L. Lebowitz, Exact results for the asymmetric simple exclusion process with a blockage, *J. Stat. Phys.* **77**, 35 (1994).
- [11] L. B. Shaw, A. B. Kolomeisky, and K. H. Lee, Local inhomogeneity in asymmetric simple exclusion processes with extended objects, *J. Phys. A* **37**, 2105 (2004).
- [12] F. Turci, A. Parmeggiani, E. Pitard, M. C. Romano, and L. Ciandrini, Transport on a lattice with dynamical defects, *Phys. Rev. E* **87**, 012705 (2013).
- [13] V. Popkov and I. Peschel, Symmetry breaking and phase coexistence in a driven diffusive two-channel system, *Phys. Rev. E* **64**, 026126 (2001).
- [14] T. Ezaki and K. Nishinari, Exact solution of a heterogeneous multilane asymmetric simple exclusion process, *Phys. Rev. E* **84**, 061141 (2011).
- [15] I. Neri, N. Kern, and A. Parmeggiani, Totally asymmetric simple exclusion process on networks, *Phys. Rev. Lett.* **107**, 068702 (2011).
- [16] T. Ezaki and K. Nishinari, A balance network for the asymmetric simple exclusion process, *J. Stat. Mech.* (2012) P11002.
- [17] E. Pronina and A. B. Kolomeisky, Theoretical investigation of totally asymmetric exclusion processes on lattices with junctions, *J. Stat. Mech.* (2005) P07010.
- [18] B. Embley, A. Parmeggiani, and N. Kern, Understanding totally asymmetric simple-exclusion-process transport on networks: Generic analysis via effective rates and explicit vertices, *Phys. Rev. E* **80**, 041128 (2009).
- [19] A. Raguin, A. Parmeggiani, and N. Kern, Role of network junctions for the totally asymmetric simple exclusion process, *Phys. Rev. E* **88**, 042104 (2013).
- [20] Y. Baek, M. Ha, and H. Jeong, Effects of junctional correlations in the totally asymmetric simple exclusion process on random regular networks, *Phys. Rev. E* **90**, 062111 (2014).
- [21] J. B. Boyce and B. A. Huberman, Superionic conductors: Transitions, structures, dynamics, *Phys. Rep.* **51**, 189 (1979).
- [22] M. B. Salamon, *Physics of Superionic Conductors* (Springer Science & Business Media, New York, 2013).
- [23] Y. Gao, A. M. Nolan, P. Du, Y. Wu, C. Yang, Q. Chen, Y. Mo, and S.-H. Bo, Classical and emerging characterization techniques for investigation of ion transport mechanisms in crystalline fast ionic conductors, *Chem. Rev.* **120**, 5954 (2020).
- [24] J. C. Bachman, S. Muy, A. Grimaud, H.-H. Chang, N. Pour, S. F. Lux, O. Paschos, F. Maglia, S. Lupart, P. Lamp, L. Giordano, and Y. Shao-Horn, Inorganic Solid-State electrolytes for lithium batteries: Mechanisms and properties governing ion conduction, *Chem. Rev.* **116**, 140 (2016).
- [25] Y. Wang, W. D. Richards, S. P. Ong, L. J. Miara, J. C. Kim, Y. Mo, and G. Ceder, Design principles for solid-state lithium superionic conductors, *Nat. Mater.* **14**, 1026 (2015).
- [26] J. Wang, T. He, X. Yang, Z. Cai, Y. Wang, V. Lacivita, H. Kim, B. Ouyang, and G. Ceder, Design principles for NASICON super-ionic conductors, *Nat. Commun.* **14**, 5210 (2023).
- [27] Y. Mo, S. P. Ong, and G. Ceder, First principles study of the $\text{Li}_{10}\text{GeP}_2\text{S}_{12}$ lithium super ionic conductor material, *Chem. Mater.* **24**, 15 (2012).
- [28] W. D. Richards, T. Tsujimura, L. J. Miara, Y. Wang, J. C. Kim, S. P. Ong, I. Uechi, N. Suzuki, and G. Ceder, Design and synthesis of the superionic conductor $\text{Na}_{10}\text{SnP}_2\text{S}_{12}$, *Nat. Commun.* **7**, 11009 (2016).
- [29] J. Maier, On the conductivity of polycrystalline materials, *Berichte der Bunsengesellschaft für physikalische* (1986).
- [30] T. Ida and K. Kimura, Ionic conductivity of small-grain polycrystals of silver iodide, *Solid State Ion.* **107**, 313 (1998).
- [31] H. L. Tuller, Ionic conduction in nanocrystalline materials, *Solid State Ion.* **131**, 143 (2000).
- [32] H. X. Zhu, S. M. Thorpe, and A. H. Windle, The geometrical properties of irregular two-dimensional Voronoi tessellations, *Philos. Mag. A* **81**, 2765 (2001).
- [33] See Supplemental Material at <http://link.aps.org/supplemental/10.1103/PhysRevResearch.6.L032032> for simulation results using other parameter values.
- [34] C. R. A. Catlow, Static lattice simulation of structure and transport in superionic conductors, *Solid State Ion.* **8**, 89 (1983).
- [35] A. Chatterjee and D. G. Vlachos, An overview of spatial microscopic and accelerated kinetic Monte Carlo methods, *J. Comput.-Aided Mater. Des.* **14**, 253 (2007).
- [36] W. Li, Y. Ando, and S. Watanabe, Cu diffusion in amorphous Ta_2O_5 studied with a simplified neural network potential, *J. Phys. Soc. Jpn.* **86**, 104004 (2017).
- [37] W. Li and Y. Ando, Effect of local structural disorder on lithium diffusion behavior in amorphous silicon, *Phys. Rev. Mater.* **4**, 045602 (2020).
- [38] H. Nakata, M. Araidai, S. Bai, H. Hirano, and T. Tada, Accurate meso-scale dynamics by kinetic Monte Carlo simulation via free energy multicanonical sampling: Oxygen vacancy diffusion in BaTiO_3 , *Sci. Tech. Adv. Mater.: Methods* **1**, 109 (2021).